Supporting Information: How structure-directing agents control nanocrystal shape: PVP-mediated growth of Ag nanocubes

Xin Qi,[†] Tonnam Balankura,[†] Ya Zhou,[†] and Kristen A. Fichthorn[*,†,‡]

Department of Chemical Engineering, The Pennsylvania State University, University Park, Pennsylvania 16802, United States

E-mail: fichthorn@psu.edu

MD Simulations

All MD simulations are carried out using a locally modified version of the LAMMPS software package.[1,2] We employ the force fields developed[2] or used[3–7] by Zhou *et al.* to characterize all interactions in the Ag-EG-PVP systems. In these force fields, the interaction of the organic molecules with the Ag surfaces was fit to results from dispersion-corrected DFT calculations.[8] For each facet type ({100} and {111} facets), a 12-layer Ag slab is placed with EG molecules and an excess amount of PVP of the desired length (PVP5mer, PVP10mer, or PVP20mer) in a simulation box with periodic boundary conditions in all directions. The in-plane dimensions of the periodic Ag slabs with EG, PVP5mer and PVP10mer are 14×14 (atoms) for Ag(100) facet and 14×16 (atoms) for Ag(111) facet. The in-plane dimensions for PVP20mer covered Ag slabs are 24×24 (atoms) for Ag(100) and 24×28 (atoms) for Ag(111).

[*]To whom correspondence should be addressed
[†]The Pennsylvania State University
[‡]Department of Physics

All simulation boxes are relaxed in the NPT ensemble using the Nosé-Hoover thermostat/barostat[9,10] at a temperature of 433 K and a pressure of 1 bar for 10 ns, and then further equilibrated in the NVT ensemble coupled with the Nosé-Hoover thermostat. The Ag-EG systems are equilibrated in the NVT ensemble for 15 ns. The equilibration times for systems with PVP are longer because of their lower mobility on Ag surfaces. Systems with PVP5mer and PVP10mer are equilibrated in the NVT ensemble for 45 ns, including 20 ns of parallel tempering using 8 replicas and temperatures ranging from 433 K to 503 K with an increment of 10 K per replica. Since the simulation box size for PVP20mer is larger than the others, systems with PVP20mer are equilibrated in the NPT ensemble for an additional 10 ns, followed by equilibrating in the NVT ensemble for 80 ns, with no parallel tempering. A time step of 1 fs is used in all MD simulations.

Subsequent to equilibration, both surfaces of the Ag slab are fully covered with PVP and excess PVP chains are distributed throughout the solution phase, suggesting that the surface coverage has saturated. "Full monolayer coverage" systems are obtained by removing all excess PVP and keeping only one of the two surfaces in the periodic cell covered with PVP. Systems with less-than-full monolayer coverage are obtained by further removing about half of PVP chains based on the full-coverage system. The numbers of chains for fully covered surfaces are 11, 7 and 10 for PVP5mer, PVP10mer and PVP20mer respectively, and the numbers for reduced coverages are 6, 4, and 7, respectively. After removing the appropriate amount of PVP chains, all systems are again relaxed in the NPT (5 ns) followed by the NVT ensemble (15 ns) using the Nosé-Hoover thermostat/barostat to ensure equilibration.

Potential of mean force calculation

To calculate the potential of mean force (PMF), we use umbrella sampling with a harmonic bias potential in a canonical MD simulation and we combine data from different windows using umbrella integration. An exhaustive description of the procedure for umbrella sam-

pling and umbrella integration is given by Kästner and Thiel.[11,12] In umbrella sampling, the system is driven from one thermodynamic state [an adsorbed Ag atom at z_f in Fig. 1(a)] to another [a free atom at z in Fig. 1(a)] along a reaction coordinate (orthogonal to the Ag surface plane) by bias potentials. A series of windows covers intermediate locations along the whole reaction coordinate. By using a moving bias potential along the reaction coordinate, the initial configurations for each window is generated, in a "pulling" simulation. The initial configuration is equilibrated for 20 ns using the Nosé-Hoover isothermal-isobaric ensemble,[9,10] followed by further equilibration in the canonical ensemble.

In the umbrella sampling process, the bias potential biases the system towards the center of the sampling window, wherein a separate region of the reaction coordinate is sampled. Overlaps in sampling between the neighboring windows are anticipated, which inspires the name of umbrella sampling. The bias potentials can be in any form, we used harmonic bias potentials for their simplicity. The harmonic bias $\omega_i(\xi)$ used has the form

$$\omega_i(\xi) = K/2(\xi - \xi_i^{ref})^2 \quad , \tag{S1}$$

where K is the harmonic force constant, ξ is the reaction coordinate, and ξ_i^{ref} is the reference point of each window i. For our model, $K = 0.7$ eV Å^{-2} is sufficient to enhance the sampling. We sampled 100 windows, with window spacing of 0.38 Å. These parameters are chosen using the guideline given by Kästner and Thiel,[13] which is

$$\Delta\xi^c < 3/\sqrt{\beta K} \quad , \tag{S2}$$

where $\Delta\xi^c$ is the minimum window spacing recommended, and $\beta = 1/k_B T$.

From umbrella sampling, the biased distribution of reaction coordinates for each window is obtained. The trajectory in each window converged after 12 ns sampling, with convergence determined by statistical tests described by Schiferl *et al.*[14] Trajectories were pre-processed by the block-average method to eliminate time correlations.[15] The PMF is computed from the

biased distributions, using umbrella integration.[11] Sufficient overlapping in the histograms of 100 windows are confirmed, which ensures that statistical errors from combining the windows are small.

Obtaining the mean-first passage time from simulation

We can obtain the mean-first passage time (MFPT) (given by equation 1) for a solution-phase Ag atom that arrives at the PVP-bulk interface to be deposited onto a Ag surface slab using quantities measurable in MD simulations.

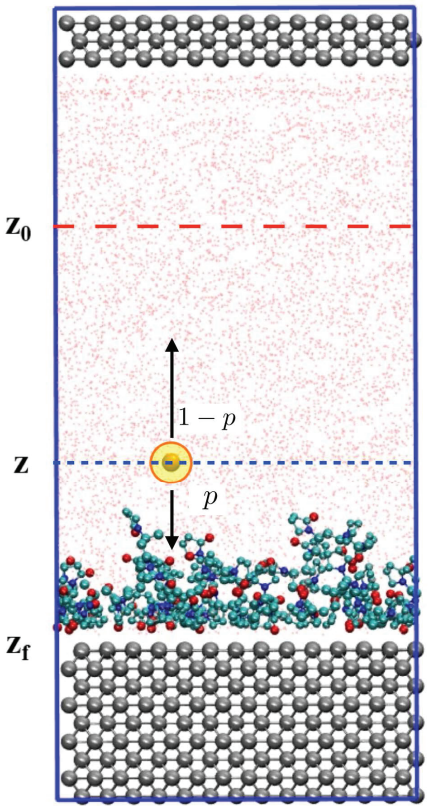

Figure S1: The demonstration of a simulation box.

The MFPT t_m is an average of the time for an atom trajectory beginning at z to reach z_f at the surface, with a reflecting boundary at z_0 that represents the interface between the bulk solution and the near-surface region, as shown in Fig. S1. As discussed in the main

text, t_m can be partitioned into a diffusion time and a reaction time. The reaction time t_R is estimated in the MD simulations, as discussed in the main text. Here, we elaborate on our estimation of the diffusion time. This is the average contribution of bulk diffusion to t_m and it accounts for multiple reflective excursions of the Ag atom to z_0 that may occur, as well as trajectories that dip below z, but turn around to the bulk solution before reaching the surface at z_f. If z lies sufficiently close to the PVP-bulk solution interface that the time associated with bulk diffusion below z is negligible compared to the time for diffusion above it, we can ignore bulk diffusion below z. In this case, the bulk diffusion time is a multiple of the time required for an atom to diffuse from z to z_0 and is given by t_D in equation 3.

Based on observations of the density profiles given below, the height of insertion z relative to the surface z_f (Fig. S1) for EG is 12 Å; the values for reduced ML coverage PVP5mer, PVP10mer and PVP20mer are 15, 16, and 17 Å, and 17, 21 and 22 Å for full ML coverage PVP5mer, PVP10mer and PVP20mer, respectively. With the height z being fixed, the inserted atom positions are chosen randomly in the xy-plane for unbiased sampling. In simulating atom deposition, four snapshots with different PVP conformations are used as initial configurations in each system. An Ag atom is inserted at a height above the PVP layer with a thermal velocity at 433 K in the direction towards the slab. Standard errors are calculated based on error propagation.

When a trajectory is initiated at z, the Ag atom proceeds to z_f before z_0 with a reaction probability of p, and returns back to the bulk phase at z_0 before z_f with a probability of $1-p$. Considering the possibility of multiple reflections from z_0, t_m is given by

$$t_m = pt_R + (1-p)p(2t_D + t_R) + (1-p)^2 p(4t_D + t_R) + \cdots \quad . \tag{S3}$$

Equation S3 consists of two geometric series, which converge to the final expression

$$t_m = \frac{1-p}{p} 2t_D + t_R \quad . \tag{S4}$$

The first term in the right-hand side of equation S4 described the total contribution of the diffusion time, and is referred to as the effective diffusion time t'_D (equation 4).

Bulk diffusivity of a Ag atom in ethylene glycol

We estimate the diffusivity of Ag atoms in bulk EG at 433 K by obtaining the mean-square displacement (MSD) of a free Ag atom as a function of time. The simulation for calculating the diffusivity of free Ag atom in EG is set up as follows. One Ag atom is placed in a simulation box with 1000 EG molecules and we simulate the system for 10 ns in the NPT ensemble at a temperature of 433 K and a pressure of 1 bar using the Nosé-Hoover thermostat and barostat.[9,10] The simulation box is further equilibrated in NVT ensemble using the Nosé-Hoover thermostat for 20 ns. Subsequent to equilibration, the production run is done in the NVT ensemble for 8 ns with position output of the Ag atom every 1 ps. Using the Ag atom trajectory output, we calculate the MSD with a time interval from 1 ps to 8 ns. We observe that the MSD is linear over the intermediate time region and we obtain the diffusion coefficient D by fitting the MSD using

$$\langle r^2(t) \rangle = 6Dt + c \quad , \tag{S5}$$

where $r(t)$ is the position of the Ag atom at time t, D is the diffusion coefficient, and c is the y-intercept of the fitted line. The production run is repeated 30 times and the average diffusion coefficient of Ag in EG is $3.3 \pm 0.2 \times 10^{-5}$ cm^2/s.

Effective Kuhn length of PVP in EG

We calculate the effective Kuhn length of PVP in EG using two methods, namely a numerical method that extracts the tangent-tangent correlation function $\langle \boldsymbol{t}_0 \cdot \boldsymbol{t}_n \rangle$ directly from simulation[17] and an analytical method based on the modified hindered rotation model.[18]

The tangent-tangent correlation function is the correlation function of the backbone vectors of the polymer. The persistence length of a polymer is obtained when the backbone tangent-tangent correlation decays to $1/e$ and the Kuhn length is twice the persistence length.

We perform a simulation to output PVP backbone carbon coordinates and backbone dihedral angles as follows. Ten atactic PVP20mer chains are put in a simulation box with a dimension of $60.0 \times 60.0 \times 95.0$ (Å), and the rest of the box is filled with EG. The system is equilibrated in the NPT ensemble at a temperature of 433 K and a pressure of 1 bar using the Nosé-Hoover thermostat and barostat.[9,10] The box is relaxed to $53.3 \times 53.3 \times 90.6$ (Å) after 5 ns equilibration in the NPT ensemble to adjust to the correct density and then equilibrated in the NVT ensemble using the Nosé-Hoover thermostat for additional 15 ns. Backbone carbon coordinates and backbone dihedral angles are output every 5 ps for a 10 ns production run. Backbone carbon coordinates are used in the numerical method and backbone dihedral angles are used in the analytical method.

When extracting $\langle \boldsymbol{t}_0 \cdot \boldsymbol{t}_n \rangle$ using the numerical method, we first obtain the PVP backbone vectors $\boldsymbol{t}_i$ from the output backbone carbon coordinates. Since the correlation between two successive vectors is governed by their bond angle, performing correlation function calculation on every backbone vector would result in decay larger than $1/e$ between the correlation of monomer index 0 (the correlation between a vector and itself) and monomer index 1 (the correlation between a vector and the next vector), which does not necessarily reflect the correct persistence length. Also, the choice of backbone vectors depends on the size of a monomer, which in the case of PVP is two carbons. Thus, instead of using successive backbone vectors, we keep the alternative backbone vectors for calculating $\langle \boldsymbol{t}_0 \cdot \boldsymbol{t}_n \rangle$. Then for each chain, we perform the dot product on backbone vectors, starting from with the correlation of a vector with itself (labelled as monomer index 0 in Fig. S2) up to the last vector to obtain the tangent-tangent correlations. The tangent-tangent correlation $\langle \boldsymbol{t}_0 \cdot \boldsymbol{t}_n \rangle$ for each monomer index n in Fig. S2 is an ensemble average of all chains from the simulation output.

We compare the result from simulation with the persistence length and Kuhn length calculated using the modified hindered rotation model.[18] By neglecting the correlations of backbone dihedral angles and assuming the bond angles are fixed at the energy minimum, we construct a transfer matrix to describe the orientation of a backbone tangent vector $\boldsymbol{t}_i$ from its neighbor vector $\boldsymbol{t}_{i+1}$. The transform matrix $\boldsymbol{T}_i$ is given by

$$\boldsymbol{T}_i = \begin{pmatrix} \cos\theta & \sin\theta & 0 \\ \sin\theta\cos\phi & -\cos\theta\cos\phi & \sin\phi \\ \sin\theta\sin\phi & -\cos\theta\sin\phi & -\cos\phi \end{pmatrix} , \tag{S6}$$

where θ is the deflection angle and ϕ is the dihedral angle of the $(i+1)^{\text{st}}$ bond. The deflection angle θ is 66.5° for PVP backbone.[4] We obtain the value of $\sin\phi$ and $\cos\phi$ by averaging the sin and cos of the dihedral angles from simulation output. Due to symmetry of the dihedral angle distribution the value of $\sin\phi$ is 0, and the value of $\cos\phi$ is calculated to be 0.428. We apply the transfer matrix with these values to predict the backbone vectors of increasing monomer index relative to the first backbone vector. We then obtain the tangent-tangent correlation function for PVP analytically, from which the persistence length is extracted.

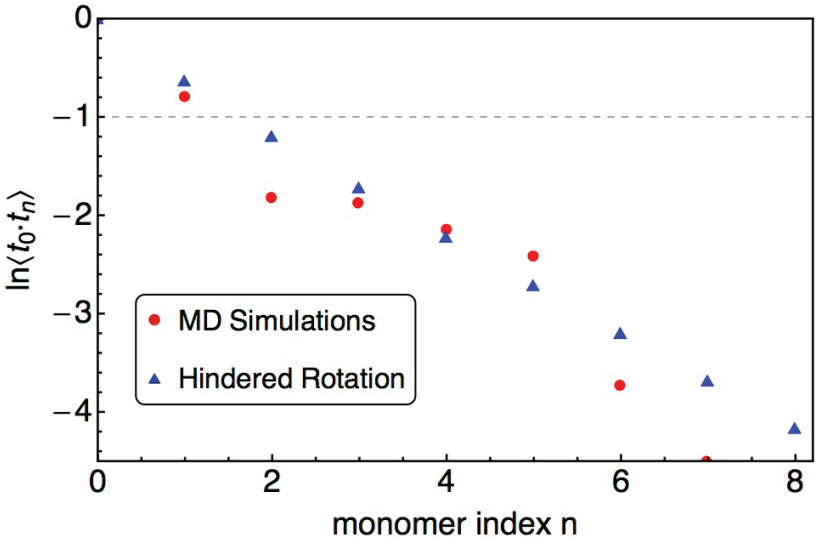

Figure S2: The tangent-tangent correlation of the PVP backbone.

The results of tangent-tangent correlation from numerical and analytical methods are shown in Fig. S2. The trends predicted by the two methods agree well with each other. The correlation decays to $1/e$ between the second and the third monomers, so by definition, we determine the effective Kuhn length of PVP in EG to be $\sim$5 repeat units.

Conformations of adsorbed PVP and density profiles

To obtain insight into how the conformations of adsorbed PVP impart different MFPTs (t_m), we construct the density profiles of O-atoms on PVP for each system studied (Fig. S3). Since each PVP repeat unit contains one oxygen atom through which the most significant PVP-Ag interaction occurs, the density profile of the O-atoms provides a measure of the PVP segment density. Generally, there are two major peaks close to the surface and smaller peaks toward the end of PVP distribution. Regarding the first two peaks: the atactic PVP used in our simulations has 2-pyrrolidone (2P) rings randomly positioned on two opposite sides of the carbon backbone. When a PVP molecule adsorbs to the Ag surfaces, it adopts a conformation in which the side with more 2P rings is closer to the surface, which leaves 2P rings on the opposite side of the backbone dangling into solution. The first (and largest) peak near the surface corresponds to the 2P rings on the side of the backbone that is closest to the surface. These oxygens adsorb directly on the Ag surface and they are closer to the Ag(100) surface due to stronger PVP-Ag(100) attraction. The second peak in the density profiles is associated with oxygen that resides in the 2P rings that dangle into solution. Differences in the overall intensity of these two peaks gives rise to the different t_R on the two surfaces.

At distances further from the first two peaks, we see smaller peaks that reflect conformational fluctuations of PVP. The PVP segments in these peaks are responsible for attracting solution-phase Ag atoms and a higher distribution of oxygen atoms in this peak indicates a greater ability in capturing free Ag atoms. As we point out in the main text, the ability to

trap Ag atoms, reflected by different values of the reaction probability p, depends on both chain length and coverage.

Chain length can affect the flexibility of polymers. We observe in simulation that PVP5mer behaves as rigid rod, and according to the result in Kuhn length calculation, it is confirmed that PVP5mer is in the rod-like regime. Thus PVP5mer lacks the semi-flexible characteristics of PVP10mer and PVP20mer. Consistent with polymer flexibility, these peaks are more observable in systems with PVP10mer and PVP20mer compared to the rod-like PVP5mer.

The influence of coverage comes from the excluded volume interaction or, more specifically, the polymer-polymer repulsion. The polymer-polymer repulsion is more significant at higher surface coverage, and stronger repulsion can result in larger conformational fluctuations. As the coverage decreases and more surface area is exposed to the solution, the lifted PVP segments caused by the polymer-polymer repulsion now can bind onto the Ag surfaces, and the conformational fluctuation subsequently reduces. Therefore, we see larger and broader peaks at full monolayer (ML) coverages than less-than-ML coverages.

Another chain length dependent effect on deposition flux is originated from the conformation inhomogeneity of PVP on Ag surfaces. The results we present in this work are obtained from the "train" conformation region. However, as seen in other studies[19] and observed here in simulations with a full ML of PVP20mer, longer PVP chains used in experiments are expected to have tails when adsorbed onto an attractive surface in good solvent. These tails appear in Fig. S3(f) as the non-flat region from approximately 17 Å to 33 Å. The number of PVP segments that reside in tails are about 5 to 7 repeat units, and the lengths of the tails are comparable on Ag(100) and Ag(111) surfaces.

The longer tails in the PVP20mer films can trap incoming Ag atoms and hold them for a long time compared to the time for the atom to access the surface in regions away from the tails. The atoms trapped in the tails eventually reach the surface, but over a much longer time scale than other deposition events, so they constitute a slow growth channel. Over

the time scale of faster deposition events, the tails will become saturated with Ag atoms, these atoms may establish an equilibrium with bulk Ag, and we do not consider this to be a significant source of the Ag surface flux. When the surface coverage of PVP decreases, more bare Ag surfaces are exposed, allowing these tails to be adsorbed on the surface. Thus, no tails are reflected in Fig. S3(e) and observed in simulations. As discussed in the main text, tails are able to attract solution-phase Ag atoms and slow down the deposition process; however, tails reflected in the density profile only contribute an insignificant portion to the entire surface, we expect that the time of deposition is predominantly determined by the train conformation regions predicted by our results.

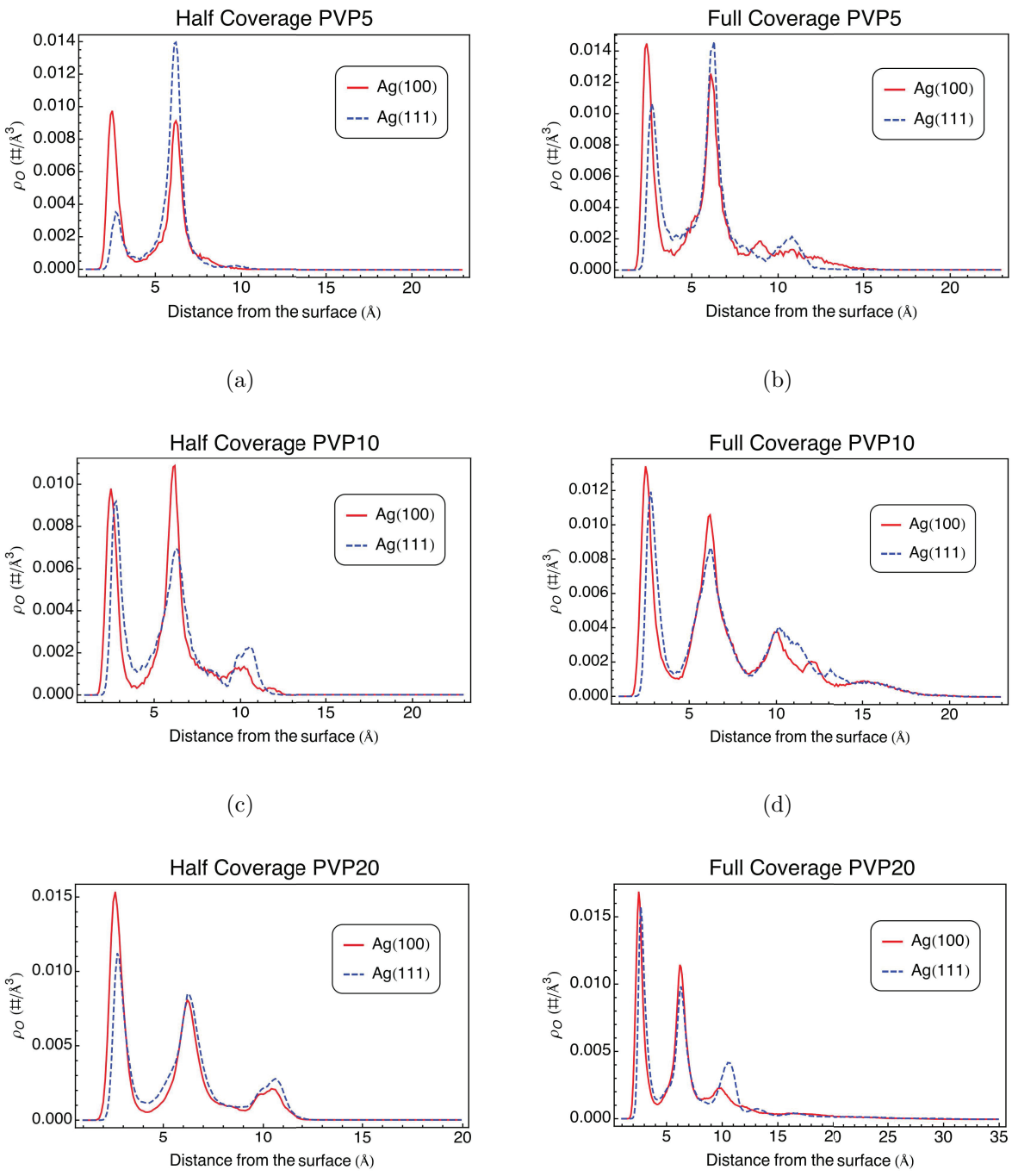

Figure S3: Density profiles of oxygen atoms on PVP of systems used in the flux simulations. Simulated systems shown above are Ag(100) and Ag(111) slabs with (a) Less-than-ML of PVP5mer, (b) ML of PVP5mer, (c) Less-than-ML of PVP10mer, (d) ML of PVP10mer, (e) Less-than-ML of PVP20mer, and (f) ML of PVP20mer in EG solution.

Kinetic Wulff plot

We use the methods described by Gadewar *et al.*[20] and Zhang *et al.*[21] to construct the kinetic Wulff plot. The nanocrystal shape contains six {100} facets and eight {111} facets. Each variation of the nanocrystal shape will have different relative sizes of the {100} and {111} facets. This allows the shapes to range from octahedra to cubes with intermediates as various forms of truncated cuboctahedra. The influence of the facet growth kinetics on the nanocrystal shape is described by equation 6 in the main text, which is used to construct Fig 4 with relative growth rates $\frac{G_{111}}{G_{100}}$ varying from 0 to 2.5. The shape calculation procedure can be summarized as follows:

1. From the defined relative growth rates, calculate the perpendicular distance x_i of each facet.

2. Extend the plane of each facet at the perpendicular distance from the shape center until it coincides with adjacent planes from other facets.

3. Three-dimensional shapes will be formed from the combination of extended planes.

4. The kinetic Wulff shape is the smallest shape formed. Note that facets with long perpendicular distance have a relatively fast growth, thus they disappear if they grow fast enough.

This method can predict steady-state shapes grown from any seed structures with valid crystallography data given that the relative facet growth rates are constant. Seeds will go through a dynamic progression to achieve the final steady-state structures. The dynamic pathway varies from the initial seed shape, but the final steady-state structure only depends on the given relative facet growth rate. Figure S4 shows an example of shape evolution

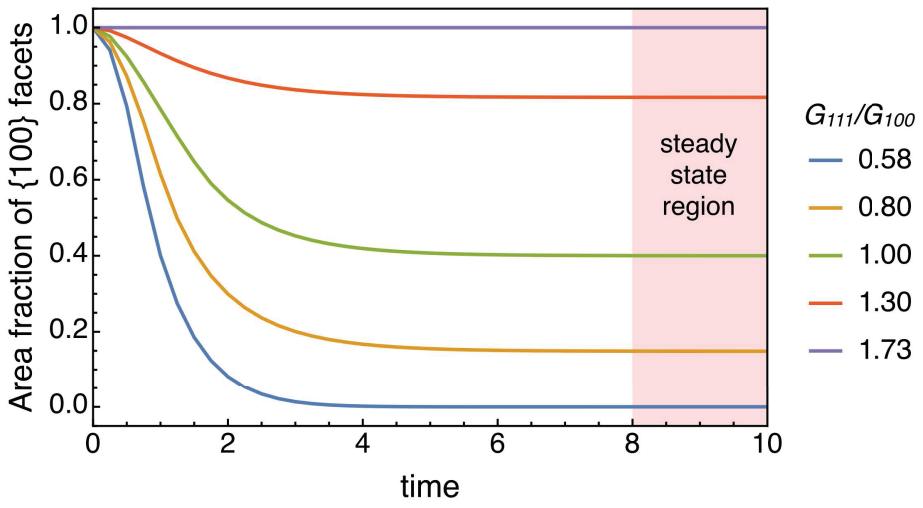

Figure S4: The dynamics of shape evolution in kinetic Wulff construction

dynamics under various relative facet growth rates. All seed structures in Fig. S4 are initially cubes.

References

(1) Plimpton, S. *J. Comput. Phys.* **1995**, *117*, 1–19.

(2) Zhou, Y.; Saidi, W. A.; Fichthorn, K. A. *J. Phys. Chem. C* **2014**, *118*, 3366–3374.

(3) Williams, P. L.; Mishin, Y.; Hamilton, J. C. *Model. Simul. Mater. Sc.* **2006**, *14*, 817–833.

(4) Vanommeslaeghe, K.; Hatcher, E.; Acharya, C,; Kundu, S.; Zhong, S.; Shim, J.; Darian, E.; Guvench, O.; Lopes, P.; Vorobyov, I.; MacKerell, A. D. Jr. *J. Comput. Chem.* **2010**, *31*, 671–690.

(5) Vorobyov, I.; Anisimov, V. M.; Greene, S.; Venable, R. M.; Moser, A.; Pastor, R. W.; Mackerell, A. D. *J. Chem. Theory Comput.* **2007**, *3*, 1120–1133.

(6) Lee, H.; Venable, R. M.; MacKerell, A. D. Jr.; Pastor, R. W. *Biophys. J.* **2008**, *95*, 1590–1599.

(7) Guvench, O.; Greene, S. N.; Kamath, G.; Brady, J. W.; Venable, R. M.; Pastor, R. W.; Mackerell, A. D. *J. Comput. Chem.* **2008**, *29*, 2543–2564.

(8) Al-Saidi, W. A.; Feng, H.; Fichthorn, K. A. *Nano Lett.* **2012**, *12*, 997–1001.

(9) Nosé, S. *J. Chem. Phys.* **1984**, *81*, 511–519 .

(10) Hoover, W. G. *Phys. Rev. A* **1985**, *31*, 1695–1697.

(11) Kästner, J.; Thiel, W. *J. Chem. Phys.* **2005**, *123*, **123**, 144104.

(12) Kästner, J. *WIREs Comput. Mol. Sci.* **2011**, *1*, 932–942.

(13) Kästner, J.; Thiel, W. *J. Chem. Phys.* **2006**, *124*, **124**, 234106.

(14) Schiferl, S. K.; Wallace, D. C. *J. Chem. Phys.* **1985**, *83*, 511–519.

(15) Allen, M. P.; Tildesley, D. J. *Computer Simulation of Liquids*; Oxford Univ. Press: New York, 1989.

(16) Xia, X.; Zeng, J.; Oetjen, L. K.; Li, Q.; Xia, Y. *J. Am. Chem. Soc.* **2012**, *134*, 1793–1801 .

(17) Colby, R. H.; Rubinstein, M. *Polymer Physics*; Oxford Univ. Press: New York, 2003.

(18) Zhang, W.; Gomez, E. D.; Milner, S. T. *Macromolecules* **2014**, *47*, 6453–6461.

(19) Linse, P.; Källrot, N. *Macromolecules* **2010**, *43*, 2054–2068.

(20) Gadewar, S. B.; Hofmann, H. M.; Doherty, M. F. *Cryst. Growth Des.* **2004**, *4*, 109–112.

(21) Zhang, Y. C.; Sizemore, J. P.; Doherty, M. F. *AIChE J.* **2006**, *52*, 1906–1915.